Ceramics International 49 (2023) 24812–24823

Contents lists available at ScienceDirect

Ceramics International

journal homepage: www.elsevier.com/locate/ceramint

Electronic structure and experimental benchmarking of aluminum spinels for solar water splitting

Francisco J. Pastor, Maxime Contreras, Teresa Lana-Villarreal, José M. Orts *, Roberto Gómez **

Institut Universitari d'Electroquímica i Departament de Química Física, Universitat d'Alacant, Apartat 99, E-03080, Alicante, Spain

ARTICLE INFO

Handling Editor: P. Vincenzini

Keywords:
Density Functional Theory
Screening
Al spinels
Water splitting
Artificial photosynthesis

ABSTRACT

A computational methodology for screening aluminum-based spinel oxides for photoelectrochemical water splitting has been developed by combining HSE06 and PBE+U calculations. The method, which can be extended to other ternary oxides, provides values for formation energies, band gaps, band edge positions, and carrier effective masses. The formation energies indicate that the Al spinels of Mg, Co, Ni, and Zn (successfully synthesized using a sol-gel method) are among the most stable in the series. Except for the Mg and Zn cases, the electronic structures of the spinels are rather similar, with band gaps separating occupied and empty 3d metal states. The charge-transfer band gap values are found to be above 3 eV, limiting the use of these materials in solar water splitting, although an estimate of the band edge positions indicates that, in general, both conduction band electrons and valence band holes can promote water reduction and oxidation, respectively. The effective masses of the charge carriers suggest that the spinels are n-type semiconductors as experimentally demonstrated. Importantly, both the UV–vis spectra and the photoelectrochemical results qualitatively agree with the theoretical electronic structure. In general vein, this work demonstrates the potential of theoretical screening for the development and selection of new photoelectrode materials based on ternary oxides for their application in solar water splitting.

1. Introduction

The serious environmental problems caused by the intensive use of fossil fuels have motivated an intensification in the research efforts devoted to developing renewable energy sources. The photoelectrolysis of water using semiconductor electrodes is one of the most interesting technologies, as it allows the conversion and storage of solar energy into chemical energy in the form of H_2 molecules [1]. For the massive application of this emerging technology, the use of elements abundant in the Earth's crust is a requisite; that is, the choice of metals is severely limited by availability and cost criteria.

So far, much research effort has been done on oxides of the first transition metal series as potential candidates for photoanodes, with some of them achieving good efficiencies [2–6], although a practical operational device is still lacking. Most of the previous work has focused on binary oxides, being lately extended to ternary and more complex oxides. A number of oxide photoanodes have been studied, including $ZnFe_2O_4$ (1.9–2.1 eV) [7], $MgFe_2O_4$ (2.0 eV) [8,9], $CuFe_2O_4$ (1.5 eV) [10], $BiFeO_3$ (2.1 eV) [11], $CuWO_4$ (2.2–2.3 eV) [12], $SnWO_4$ (1.64–2.1 eV) [13], and Fe_2WO_6 (1.5–1.7 eV) [14,15]. All of them show a very limited efficiency due to high electron-hole recombination rates both at the surface and in the bulk. The most promising ternary oxide seems to be $BiVO_4$ (2.4–2.5 eV), which has a slow electron-hole bulk recombination rate, leading to considerable photocurrents. Its main limitation, together with a relatively low stability, is a rather wide band gap and a short hole diffusion length [16–20].

Only a few ternary oxides have been observed to behave as photocathodes [21]. In this respect, $YFeO_3$ (2.45 eV), $LaFeO_3$ (2.0–2.7 eV), $CaFe_2O_4$ (1.85 eV), and $CuFe_2O_4$ (2.1 eV) have very low carrier mobilities [22–25]. On the other hand, $CuFeO_2$ shows detrimental surface states and $CuCrO_2$ a too wide band gap [26,27]. There is still much progress to be made with ternary oxides, and taking into account that the number of those included in the ICSD database amounts to 10,350, it is not feasible to experimentally test in a systematic way all of them in the search for the most promising ones [28]. Woodhouse et al. applied an advantageous methodology for the experimental screening of quaternary oxides of cobalt, aluminum and iron. They prepared different oxide compositions on an FTO substrate by using an ink-printing

* Corresponding author.
** Corresponding author.
E-mail addresses: jm.orts@ua.es (J.M. Orts), roberto.gomez@ua.es (R. Gómez).

https://doi.org/10.1016/j.ceramint.2023.05.003
Received 18 September 2022; Received in revised form 14 April 2023; Accepted 1 May 2023
Available online 2 May 2023

deposition technique, and measured their photoresponse, to conclude that the $Co_{3-x}Al_xFe_yO_4$ (x = 0.18; y = 0.30) spinel, with a bandgap of 1.5 eV, had the largest photoresponse for water photoelectrolysis among the cobalt aluminum iron oxides [29].

In general, spinel type oxides are materials adequate for solar water splitting because of their good optical and mechanical properties, as well as high stability against corrosion. For RAl_2O_4 (R: Mg, Ti–Zn), many experimental works are found in the literature. The $MgAl_2O_4$ spinel has a high melting point, high hardness, low density, high mechanical strength, high electrical resistivity, and an experimental direct band gap of 7.8 eV. Other values have been reported, depending on the inversion degree and stoichiometry deviation [30,31]. As far as we know, there are no publications on $TiAl_2O_4$ and VAl_2O_4, while one paper has been published on $CrAl_2O_4$, presenting its synthesis in a reductive atmosphere [32]. Wang et al. reported for $MnAl_2O_4$ band gaps varying from 2.5 to 1.6 eV as the annealing temperature increases, which is attributed to a decrease in the content of amorphous alumina [33], while Saguna et al. reported a direct band gap of 4.04 eV for this material [34]. Mu et al. found an experimental indirect band gap of 1.78 eV for $FeAl_2O_4$ [35]. Boudiaf et al. reported a direct band gap of 1.83 eV for $CoAl_2O_4$ [36], while other groups gave direct band gap values of 2.9–3.6 [34,37–40]. Sebai et al. measured a direct band gap of 1.84 eV for $NiAl_2O_4$ [41], whereas other authors reported values in the range from 2.9 to 3.5 eV [37,38,42–46]. For $CuAl_2O_4$, values from 1.77 to 3.0 eV can be found in the literature [44,47–55]. Finally, for $ZnAl_2O_4$, the band gap values are reported to range from 4.2 to 5.50 eV [44,56,57]. In general, there is a significant variability in the reported band gap values, probably due to different degrees of inversion and stoichiometry deviations in the synthesized materials [30].

Importantly, the enormous increase in computational power in recent years has allowed for a computational screening in which a series of fundamental properties of semiconductors are evaluated, for instance in the search of candidates for water photoelectrolysis. Castelli et al. published papers using this methodology on perovskite metal oxides, oxynitrides, oxysulfides, and oxyfluorides [58,59], on double perovskite oxides (combination of two simple perovskites) [60], and on layered perovskite oxides and oxynitrides [61]. In all cases, stability, band edge positions, and band gaps were evaluated. Kuhar et al. evaluated for perovskite sulfides, crystalline structure, stability, band gaps and effective masses, as well as tolerance to sulfide vacancies [62]. Pandey et al. published a theoretical screening of quaternary chalcogenides focused on stability, band gap, and effective masses [63]. Band gaps are evaluated with the GLLB-SC functional of the GPAW code, which gives accurate values for non-magnetic materials, although it does not allow for geometry optimization. Wu et al. studied the stability, band gap, and band edge positions of nitride and oxynitride photocatalysts [64]. Xu et al. looked for layered double hydroxide photocatalysts for the oxygen evolution reaction, and calculated their electronic structures, band structures, and band edge positions [65]. In the two latter works, band gaps were evaluated with the PBE+U method, which gives accurate values for highly correlated magnetic materials. Recently, computational screening of single layer metal chalcogenides at the HSE06 level has been performed to evaluate their performance as photocatalysts for water splitting [66,67]. Jain et al. have carried out a complete study in the search of new materials (based on oxide, sulfide, and fluoride anions and their combinations in binary, ternary and quaternary materials) with novel or interesting properties [68]. This study was carried out with PBE+U, with optimal values of U obtained by comparison with the experimental formation energies from the corresponding binary oxides. Finally, Aykol et al. obtained U values as a function of the oxidation state of the transition metal and the nature of the anion (O^{2-} and F^{-}), using the formation energies of the binary oxides as a reference. [69].

In this paper, a method is proposed for the computational screening of some aluminum-based spinels, which could be potentially extended to other ternary oxides. The methods beyond DFT used here (DFT+U and hybrid functionals) rely on some empirical parameters, such as the alpha mixing and the Hubbard parameters, whose values must be adjusted taking as a reference experimental data. They are strongly dependent on the oxidation state and the environment of the transition metal in the structure. In the bibliography, studies can be found delivering values for these parameters for various transition metal oxides, taking as a reference the formation energies of oxides and fluorides [68], the formation energies of binary and ternary oxides [69,70], the electronic structure, and the band gap [71]. However, a systematic study of these parameters for the first period transition metals with oxidation state +2 and tetrahedral coordination is still lacking. Here, we have carried out the tuning of the HSE06 mixing parameter as to reproduce the experimental band gaps. A subsequent tuning of the Hubbard parameter is implemented for each spinel as to reproduce with the PBE+U method the electronic structure and band gaps obtained from the HSE06 calculations. With these values for the mixing and Hubbard parameters for the metals in the RAl_2O_4 series, a computational screening at the PBE+U and HSE06 theory levels has been performed, focused on the estimation of properties such as band gap, band edge positions, and effective masses of the charge carriers. On the experimental side, optical and photoelectrochemical measurements have been carried out to test the performance of these RAl_2O_4 spinel materials as photoelectrodes in photoelectrochemical water splitting. Finally, theoretical and experimental results are compared as to evaluate both the soundness of the computational approach and the potential for application of the oxides in the series.

2. Materials and methods

2.1. Computational details

DFT calculations have been performed with the Vienna Ab initio Simulation Package (VASP) [72], using the projector augmented wave (PAW) method [73,74] at the PBE [75], PBE+U (following the approach of Dudarev [76]) and HSE06 theory levels. All calculations were done with a plane-wave energy cutoff of 520 eV, except for the HSE06 case, where the plane-wave energy cutoff was 400 eV. Spin-polarized calculations were carried out for all spinels with the magnetic moments arranged initially in either a ferromagnetic or an antiferromagnetic configuration. For each material, the spin arrangement leading to the lowest energy was selected for all the subsequent calculations.

The GGA functional parametrized by Perdew, Burke and Ernzerhof (PBE) has a well-documented tendency to significantly underestimate the value of the band gap [71]. Better estimates of this value can be obtained by introducing the Hubbard correction (in the PBE+U calculations), which aims to account for the electronic correlation of the highly localized d-electrons in transition metal oxides. Even better estimates of the band gap and other properties can be obtained using the range-separated hybrid HSE06 functional [77]. The results obtained with this functional are affected by the value of the mixing parameter α (which determines the fraction of exact Fock exchange to be included in the calculation). It is important to note that we define the fundamental band gap as:

$$E_g^f = E_{min}^{LUMO} - E_{max}^{HOMO} \quad (1)$$

where, E_{min}^{LUMO} is the energy at the minimum of the first empty band and E_{max}^{HOMO} is the energy at the maximum of the uppermost band filled with electrons.

Insulating 3d-electron systems can be of two types. In Mott-Hubbard (MH) insulators, the band gap is due to by the splitting of the 3d shell, while, for charge-transfer (CT) insulators, the band gap separates the occupied p bands of oxygen and the unoccupied 3d shell of the metal [78].

Fig. 1 shows the flowchart followed to obtain the adjusted (or tuned) empirical parameters: α (for the HSE06 theory level) and the Hubbard parameter, U, for Dudarev-type PBE+U calculations. Following the

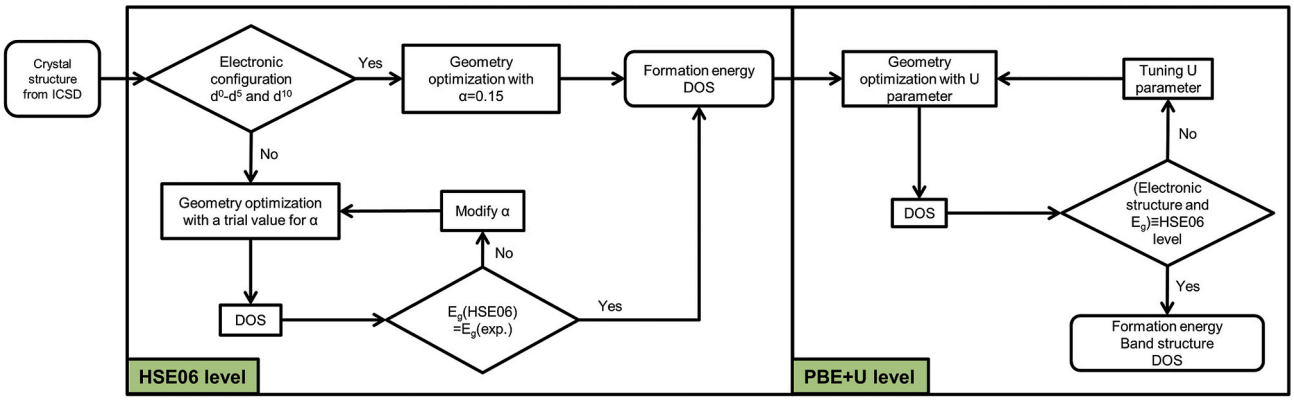

Fig. 1. Flowchart of the DFT calculations carried out for tuning the empirical parameters α and U, and for screening the RAl_2O_4 (R: Mg, Ti–Cu) series.

criteria by He et al. [71], a value of 0.15 was used for the Al-spinels of Mg, Ti, V, Cr, Mn and Zn (with d^0, d^2, d^3, d^4, d^5 and d^{10} configurations for the respective metal centers), while for the Al spinels of Fe, Co, Ni and Cu (d^6, d^7, d^8 and d^9 configurations, respectively), the mixing parameter has been adjusted. For the metals in the series from Fe to Cu, there are enough experimental data on band gaps, including the data reported in this paper for Co and Ni, which agree with values reported by other groups [34,37–46]. These data allow us to adjust the α value (with ±0.05 steps except for the case of Ni, where ± 0.01 steps were used) as to obtain fundamental band gap values calculated with HSE06 that satisfactorily agree with the experimental ones. Once the electronic structure (DOS) and band gap are available at the HSE06 level for all the spinels, the adjustment of the Hubbard U parameter (PBE+U) is carried out (in steps of ±0.1 eV) to reproduce them.

With the PBE+U approach, it is not always possible to reproduce simultaneously the electronic structure (DOS) and the band gap. In some cases, to reproduce the band gap, it is necessary to use very high U values, which causes distortion of the electronic structure. In this work, we have adopted as a master criterion the reproduction of the electronic structure (obtained at the HSE06 level), this prevailing over the gap value. Once all the empirical parameters are adjusted to their optimal values, the structures are optimized and the formation energies (from the respective binary oxides), the DOS, and the band structure are obtained.

The U and α parameters obtained in the tuning steps are given in Table 1, together with some U data reported by other groups (for the sake of comparison) [68]. For the metal electronic configurations from d^0 to d^5 as well as for d^{10}, the value of α was fixed at 0.15, and the tuned U values tend to decrease as electrons are added to the d shell. Subsequently, for configurations with more than 5 d electrons (high spin), as additional electrons are introduced in the e subshell, both α and U decrease and, finally, when further electrons are added to the t_2 subshell, both α and U progressively increase.

For the binary oxides and spinels, the experimental crystalline structures of the most stable phases have been obtained from the Inorganic Crystal Structure Database (ICSD). For the spinels, they correspond to the standard primitive normal spinel cell (SG number 227) (with a total of 14 atoms, see Fig. 2). In the cases of the Ti and Cr spinels (with no ICSD structure file), the initial guess structure was the ICSD structure for VAl_2O_4. Fig. 2 also shows the antiferromagnetic arrangement adopted for the transition metals in the spin-polarized calculations.

Table 1
Values for the U and α parameters obtained from the tuning step for all R^{2+} transition metals in a tetrahedral coordination and used in the screening step for the PBE+U and HSE06 calculations, respectively. Data from ref. 68 are also given for comparison.

	Ti	V	Cr	Mn	Fe	Co	Ni	Cu
U/eV [68]	0.0	3.1	3.5	3.9	4.0	3.4	6.0	4.0
U/eV	3.7	3.1	3.3	3.0	2.1	1.4	3.3	6.7
α	0.15	0.15	0.15	0.15	0.10	0.05	0.12	0.20

2.2. Experimental details

Analytical grade nitrates of the transition metals ($R(NO_3)_2{\cdot}xH_2O$; purity >98% in all cases) (see more details in the Supplementary data, Table S1), and aluminium nitrate ($Al(NO_3)_3{\cdot}9H_2O$, (Sigma–Aldrich,>98.5%)) were mixed in a 1:2 mol ratio and dissolved in deionized water (Millipore, 15 MOhm·cm) under magnetic stirring for 15 min. Subsequently, citric acid ($HOC(COOH)(CH_2COOH)_2$; Sigma–Aldrich, >99%) was added to the solution in a 3:4 metal:citric acid mole ratio. After stirring for 30 min, a concentrated aqueous ammonia solution (Labkem, 30%) was added dropwise to adjust the pH to 7.0 and the resulting solution was kept at 90 °C until a gel was formed, which was then dried at 150 °C overnight. The dried gel was thermally treated at 1100 °C for 1 h in air to obtain a powder [47].

With this sol-gel procedure, the pure phases (as deduced from XRD measurements, *vide infra*) of the Al-spinels of Mg, Co, Ni, and Zn were successfully synthesized. The Al spinels of Mn, Fe, and Cu were also obtained, although the solids contained significant amounts of their respective binary oxides.

For the UV–vis band gap measurements, the spinel powder was deposited over either an F:SnO_2-coated glass (FTO, Pilkington TEC15) substrate (in the case of the Al spinels of Co and Ni) or a quartz substrate (for the Al spinels of Mg and Zn). Films on substrates have been made by doctor blading [25]. The optical properties of the films were studied by solid-state UV–vis spectroscopy, using a Shimadzu UV-2401 PC spectrophotometer equipped with an integrating sphere and working in the diffuse reflectance mode.

X-ray diffractograms of the spinel films were obtained with a Bruker D8-Advance system, using the Cu Kα radiation with a step scan of $1^\circ{\cdot}min^{-1}$.

Photoelectrochemical measurements were performed at room temperature in a home-made Pyrex glass cell with a fused silica window and a computer-controlled potentiostat-galvanostat (Autolab, PGSTAT30). A Pt wire and an Ag/AgCl/KCl(3 M) electrode were used as counter and reference electrodes, respectively. An N_2-purged 0.1 M NaOH (Panreac, 98.0%) solution was used as an electrolyte. The light source was an ozone-free 1000 W Xe(Hg) arc lamp (Newport Instruments) equipped with a water filter to minimize the infrared contribution of the beam. Unless otherwise stated, the photoelectrochemical measurements were carried out by irradiating the electrodes through the electrolyte/electrode interface (EE illumination).

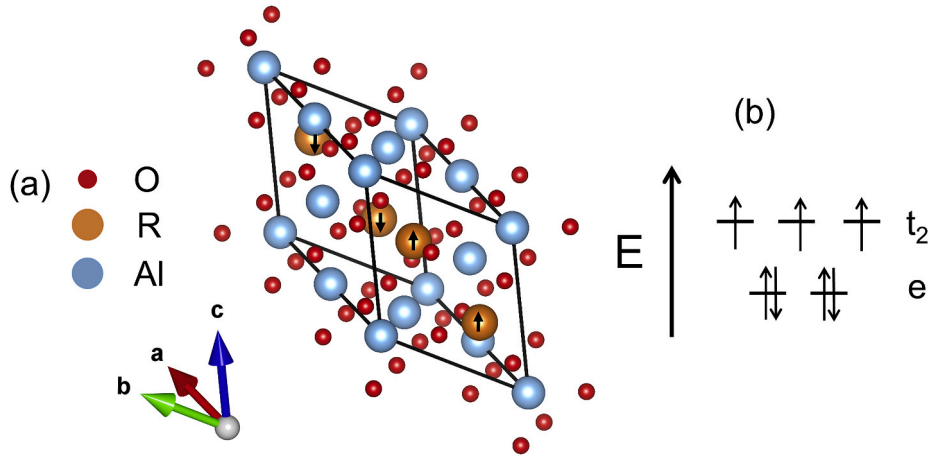

Fig. 2. (a) Standard primitive normal spinel cell (SG 227), showing the antiferromagnetic ordering considered in the calculations. (b) Scheme of the d-state energy splitting according to the crystal field theory for a transition metal cation (Co^{2+}, d^7 as an example) in a tetrahedral environment.

3. Results and discussion

3.1. Formation energies

The formation energy of the spinels from their respective binary oxides was calculated for two purposes. First, to check whether the different theory levels lead to similar and consistent values for each of the oxides considered and, second, to identify those ternary oxides that are unlikely to form a stable spinel phase.

Fig. 3 shows the formation energies of the RAl_2O_4 spinels from Al_2O_3 and the binary R oxide evaluated as described in the Supplementary data (section S1). The tolerance factor is also plotted and it was evaluated according to [79]:

$$t = \frac{\sqrt{3}(R_{Al} + R_O)}{2(R_R + R_O)} \quad (2)$$

where R_{Al}, R_O and R_R are the ionic radii for Al, O, and R in the RAl_2O_4 spinel.

The formation energy values at the PBE level tend to be too high, except for the case of Mg (empty d shell), Mn (filled α-spin subshell and empty β-spin subshell) and Zn (filled d shell). In all the other cases, the formation energy at the PBE+U and HSE06 levels is always lower than at the PBE level. For Ti, V, Ni, and Cu, the formation energy at the PBE+U level is lower than at the HSE06 level, while for Cr, Fe, and Co the trend is reversed. If we compare the formation energies obtained for the spinels of Mg (at the PBE level), Fe (at the PBE+U level), and Zn (at the PBE level) with the calculated and experimental formation energies reported by Hautier et al. [70], a good agreement is found. This can be taken as an indication that the methodology used is correct. According to the formation energy values, we can distinguish three different groups: spinels with large positive values (Ti, V and Cr), spinels with moderate positive values (Ni and Cu), and spinels with negative values (Mg, Mn, Fe, Co, and Zn).

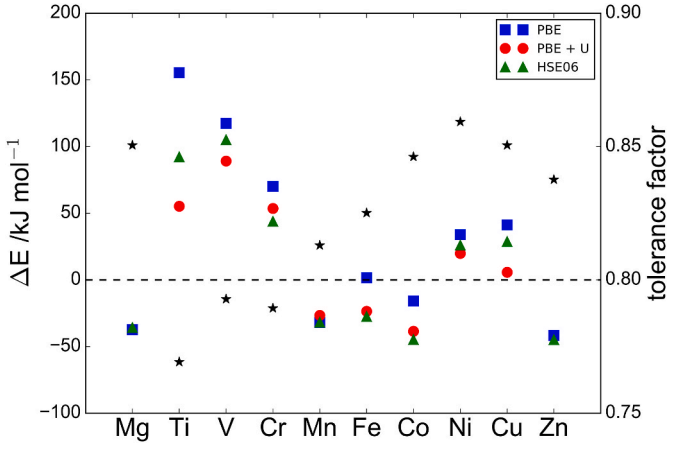

Fig. 3. Calculated formation energies for the RAl_2O_4 spinels (R = Mg, Ti–Zn) from the binary oxides, obtained at the PBE, PBE+U, and HSE06 theory levels. The stars correspond to the tolerance factor values.

For all the studied spinels, the tolerance factors are lower than 1. This is because we have only considered the normal spinel structure, in which the octahedral site is occupied by Al^{3+}, whose radius is very small. For the Ti, V, and Cr spinels (large positive formation energy), tolerance factors below 0.80 are obtained because the transition metal ions are too large for the tetrahedral sites. Otherwise, the size of the transition metal is adequate for the tetrahedral site. Ni and Cu spinels have a moderate positive formation energy, attributed to the fact that our calculation only refers to normal spinels, without consideration of the inverse structure, which is reported as the thermodynamically stable phase. The $NiFe_2O_4$ spinel has a high degree of inversion and the normal phase only forms under very specific conditions (high temperature) [80], while the $CuAl_2O_4$ has a lower degree of inversion [81].

3.2. Density of states

In this section the electronic structure of the Al spinels is discussed as a function of the theory level applied for the calculations. Fig. 4 shows the DOS plots obtained at the HSE06 and PBE+U theory levels with the tuned values for the α and U parameters. For the sake of comparison, Fig. S1 shows the DOS for the spinels as determined at the PBE theory level, while Figs. S2–S6 show the information given in Fig. 4 and Fig. S1 organized in an alternative way for a better visualization.

The DOS plots in Fig. 4 show a similar electronic structure pattern for all the spinels in the series (except for those of Mg and Zn). From negative to positive energies, one finds an O 2p block, a metal 3d block just below the Fermi level (with filled bands) and, above the fundamental band gap, another metal 3d block (with empty bands). In these blocks the hybridization with electronic states of other atoms is very weak, which indicates that these are strongly ionic spinels. Finally, at higher energies, we have a block of highly hybridized O 2p and R 3d states. In other words, in most cases the band gap is fundamentally defined by states that come from the transition metal, and it is the crystal-field energy-splitting effect on the transition metal d-states what defines the width of the band gap. Under these circumstances, the value of the U parameter (which only affects the d electrons) strongly

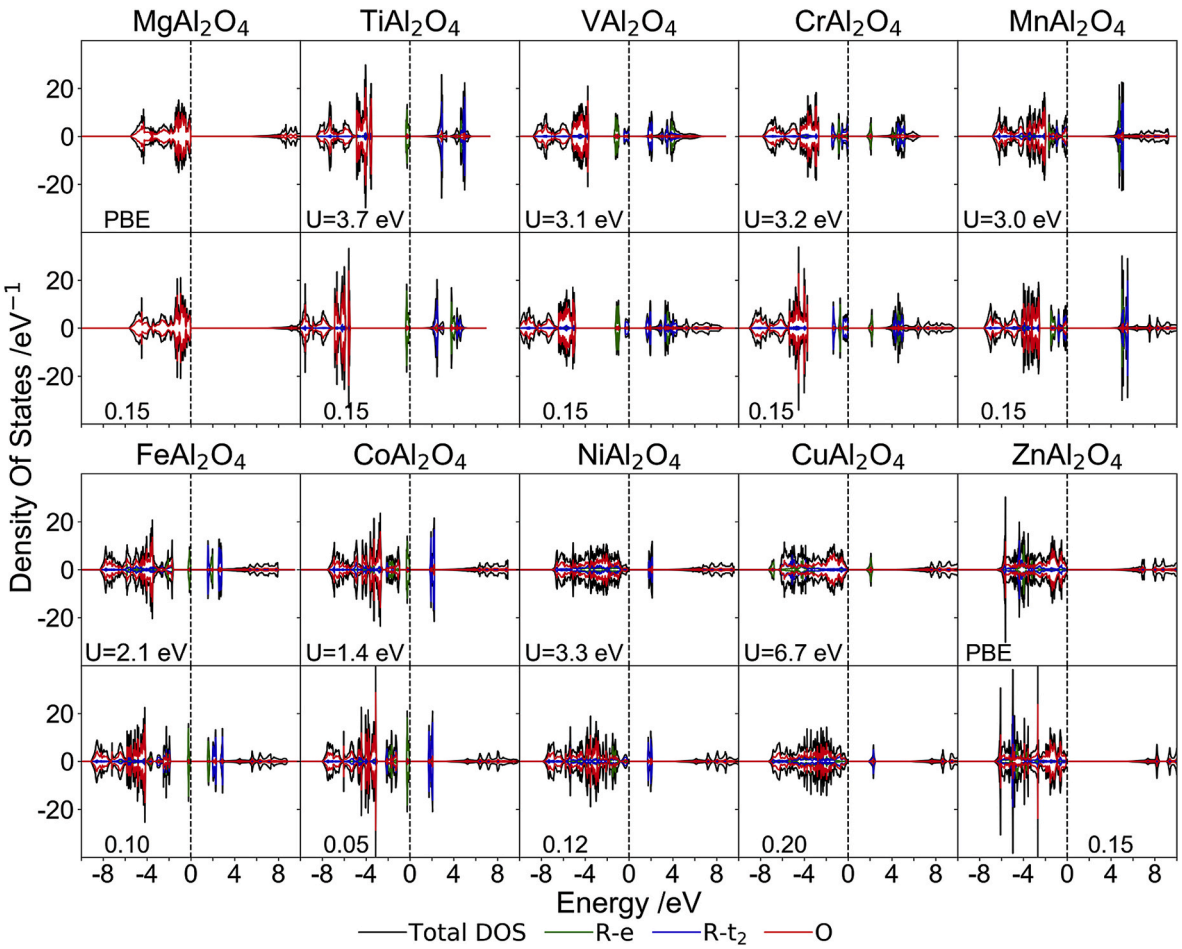

Fig. 4. Total and partial DOS for the RAl_2O_4 spinels (R: Mg, Ti–Zn), calculated at the theory levels: PBE+U (top rows of panels) and HSE06 (lower rows of panels). The adjusted U and α values are also given.

influences the value of the band gap. It is worth noting that, for all the transition metals (except for Mn), it has been possible to find a U value that reproduces simultaneously both the electronic structure and the band gap at the HSE06 level. In the case of materials with a high degree of hybridization between the transition metal d states and the 2p states of oxygen, very high U values may be needed to reproduce the experimental band gap, causing a significant distortion of the electronic structure [82].

The spinels $MgAl_2O_4$ and $ZnAl_2O_4$ are diamagnetic band insulators. Li et al. and Phatak et al. reported PBE band gap values for $MgAl_2O_4$ of 5.41 eV and 6.0 eV, respectively. Li et al. reported a band gap of 7.53 eV obtained with HSE06 (and 35% of HF exchange). The latter value is close to the experimental band gap of 7.8 eV [30,31]. For $ZnAl_2O_4$, experimental band gap values of 5.50 [44], 5.45 [57], and 4.2 eV [56] have been recently reported. For these spinels, we have obtained the same main contributions to the valence and conduction bands irrespective of the theory level used. The band gap of the $MgAl_2O_4$ spinel separates the edge of the valence band constituted by O 2p states from the edge of the conduction band constituted by Mg 3s and Al 3s empty states hybridized with O 2p states. Interestingly, there exists a good agreement between the electronic structure of $MgAl_2O_4$ shown in Fig. 4 and valence-band XPS measurements for this material [83]. For $ZnAl_2O_4$, calculations give an edge of the valence band formed by O 2p states, while the edge of the conduction band is formed by O 2p states hybridized with Zn 4s empty states.

Fig. S7 shows the PBE+U DOS obtained with U values in line with those reported in the literature [68]. For V, Cr and Mn, the adjusted U values (used for generating Fig. 4) practically coincide with those that appear in Fig. S7, resulting in the same band gaps. On the other hand, for Fe, Co, Ni, and Cu, the adjusted U values differ significantly from those in Fig. S7. The band gap values (and band gap type) found in both the literature and our calculations (Fig. 4) for the different spinels are gathered in Table 2.

All the theory levels used in this work predict that the Fe and Co spinels have a Mott-Hubbard type band gap, and that the Mn, Ni, and Cu spinels exhibit a mixed Mott-Hubbard charge-transfer behavior. The agreement between the calculated DOS (with PBE+U and HSE06) of $CoAl_2O_4$ and experimental valence-band XPS and O K-edge spectra is remarkable [84], while for $NiAl_2O_4$ and $CuAl_2O_4$ spinels the agreement with experimental valence-band XPS is not optimal [51,52,85,86]. In fact, according to the electronic structures calculated for the latter, substantial hybridization in the valence band between O 2p states and metal 3d states should occur, although the profile shown by the valence-band XPS does not indicate such a high degree of hybridization.

3.3. Band structure and effective masses

Fig. 5 shows the band structure for the studied Al spinels, obtained at the PBE+U level. The calculated effective masses for the charge carriers obtained from these band structures are reported in Table 3. In the case of the Mg and Zn spinels, a direct transition centered at the Γ point is obtained, with a very flat valence band in all the k-space, while the conduction band minimum is very deep. The Mg and Zn spinels have a highly isotropic electrical conductivity, mainly due to conduction band electrons, as they have effective mass values around a twelfth and a fifth that of the holes in the valence band, respectively. Such a large

Table 2
Experimental band gaps, calculated band gaps (from the literature), and band gaps calculated in this work (fundamental band gap and charge-transfer band gap) for the RAl_2O_4 spinels.

Spinel	Experimental band gap/eV	Calculated band gap/eV (literature)	Fundamental band gap/eV			Band gap type	Minimum CT band gap
			PBE	PBE+U	HSE06		
$MgAl_2O_4$	7.8 [30,31]		5.2	–	6.8	B	–
$TiAl_2O_4$			0.02	0.94	0.97	MH	4.4
VAl_2O_4			0.02	1.1	1.3	MH	4.7
$CrAl_2O_4$			0	1.7	1.8	MH	4.9
$MnAl_2O_4$	4.4 [34]	2.21 (U = 2 eV) [87]	2.4	3.0	3.7	MH/CT	3.0
$FeAl_2O_4$	1.78 [35]	1.77 (U = 2.5 eV) [35]	0.07	1.5	1.5	MH	3.4
$CoAl_2O_4$	FBG: 1.8 [36]	FBG: 1.78 (U = 2 eV) [87,88]	0.87	1.8	1.7	MH	3.8
	CTBG: 3.04–3.6 [34,37,38]	FBG: 2.32 (U = 3 eV) [88]					
$NiAl_2O_4$	FBG: 1.84 [41]	FBG: 2.3 (U = 2.8 eV) [80]	0	1.8	1.8	MH/CT	3.5
	CTBG: 3.0–3.45 [37,38,42,44]	FBG: 3.9 (U = 6.4 eV) [80]					
$CuAl_2O_4$	FBG: 1.7–2.3 [47–52]		0	1.7	1.8	MH/CT	4.3
	CTBG: 3.0–3.75 [44,51,52]						
$ZnAl_2O_4$	4.2–5.5 [44,56,57]		3.9	–	5.1	B	–

Band gap type and minimum charge-transfer band gap have been evaluated at the PBE+U level. All the minimum charge-transfer band gaps are direct and correspond to the Γ point. FBG: fundamental band gap; CTBG: charge-transfer band gap; MH: Mott-Hubbard insulator; CT: charge-transfer insulator; B: diamagnetic band insulator.

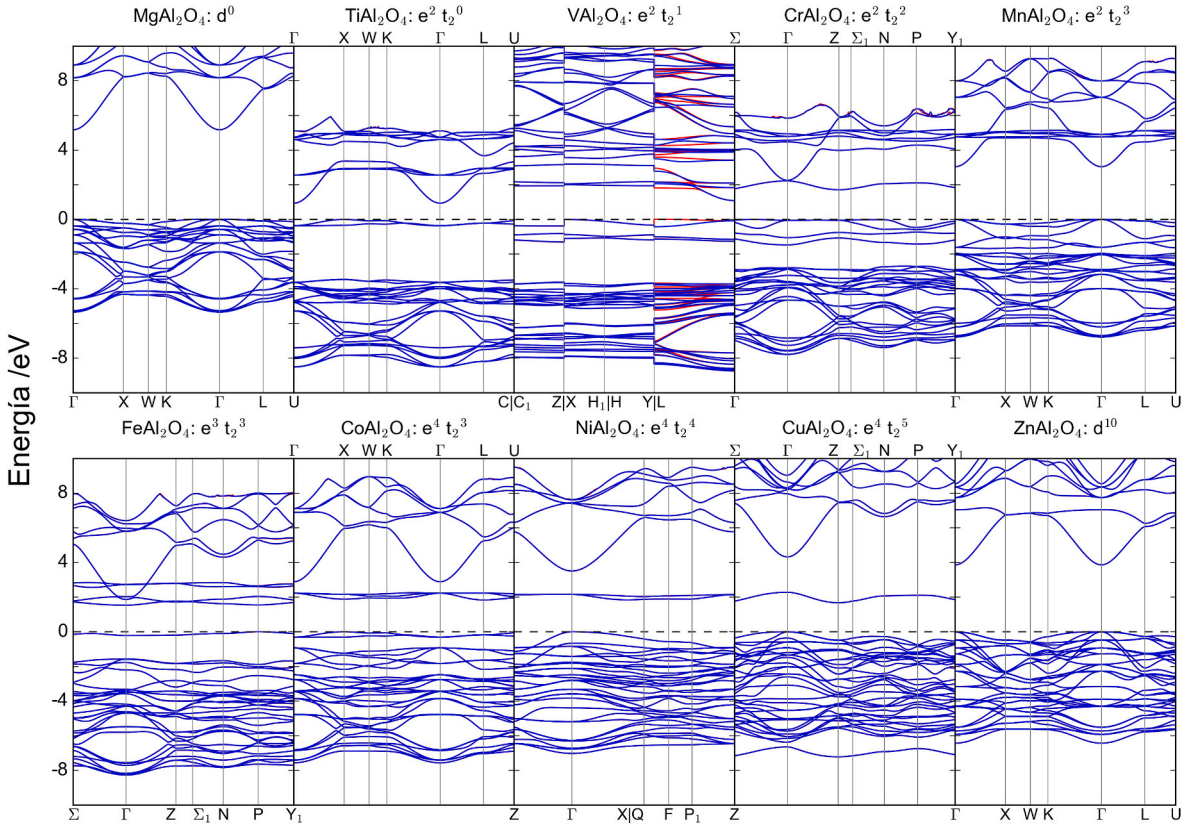

Fig. 5. Band structures for the RAl_2O_4 spinels at the PBE+U level (blue: spin α; red: spin β; both coincide except for VAl_2O_4). (For interpretation of the references to color in this figure legend, the reader is referred to the Web version of this article.)

difference in effective masses suggests an n-type behavior for undoped nanostructures of these two spinels. In this respect, it should be kept in mind that the prediction of the n- or p-type behavior of a semiconductor electrode is only partly based on the mobility of the carriers (in the case of nanoporous electrodes), but rather on their densities. These densities result, particularly in the case of oxides, from deviations of the expected stoichiometry that occur non-intentionally during the materials' synthesis.

The $TiAl_2O_4$, VAl_2O_4 and $CrAl_2O_4$ spinels have, respectively, X→ Γ, N → Γ and N →Z indirect gaps. These three spinels have a fundamental Mott-Hubbard type band gap. In addition, charge-transfer type band gaps of 4.40 eV, 4.70 eV, and 4.91 eV, respectively, all located at the Γ-point, are also predicted. In the case of the Ti and V spinels, their conduction bands are made up entirely of empty 3d transition metal states, and span over a wide range of energies, with a very deep minimum at the Γ point. This implies that the 3d empty states of the transition metals overlap and hybridize with each other, yielding a conduction band with a very low effective mass for the electrons.

In the case of the Cr spinel, the lower empty band is also made up entirely of Cr 3d states, whose energy changes very weakly throughout the k space. Therefore, they give rise to very large electron effective masses. In addition, at the Γ point, there is another band that forms a very sharp minimum with the same energy as the first conduction band. The effective mass for the electrons in this band is only of $0.39m_e$. For Ti,

Table 3
Effective masses of electrons and holes obtained for fundamental band gaps (with Boltztrap2 model) and for charge-transfer band gaps (with the parabolic model) for the RAl_2O_4 spinels evaluated at the PBE+U level.

Spinel	From band edges for fundamental band gap						From band edges for CT band gap	
	m_e^*/m_e			m_h^*/m_e				
	x	y	z	x	y	z	m_e^*/m_e	m_h^*/m_e
$MgAl_2O_4$	0.41	0.41	0.41	4.87	4.87	4.87	–	–
$TiAl_2O_4$	0.43	0.39	0.39	6.10	4.25	4.25	0.40	0.80
VAl_2O_4	0.41	0.41	0.41	17.5	2.60	2.72	–	–
$CrAl_2O_4$	2.41	2.41	2.79	2.17	2.17	108.4	0.39	–
$MnAl_2O_4$	0.40	0.40	0.40	4.21	4.21	4.21	–	–
$FeAl_2O_4$	13.1	10.75	8.31	11.55	4.70	50.3	0.39	–
$CoAl_2O_4$	5.11	5.11	5.11	5.54	5.54	5.54	0.40	0.66
$NiAl_2O_4$	20.87	5.58	6.10	0.66	3.35	2.53	0.39	–
$CuAl_2O_4$	2.28	2.28	2.38	2.65	2.64	1.81	0.39	–
$ZnAl_2O_4$	0.39	0.39	0.39	1.93	1.93	1.93	–	–

V and Cr spinels, the electrical conduction is expected to be mainly sustained by electrons (hole effective masses several times greater than electron ones), which suggests an n-type character for undoped nanostructures of these spinels.

Fig. 5 also shows a direct band gap at the Γ point for $MnAl_2O_4$, with a relatively flat valence band throughout the entire k space, and a very sharp minimum in the conduction band. The calculated effective masses (Table 3) indicate that this spinel is a good isotropic electric conductor, conduction band electrons being the main charge carriers, with an effective mass more than ten times smaller than that of holes in the valence band. A P → Γ indirect band gap for $FeAl_2O_4$ and an X→L indirect band gap for $CoAl_2O_4$ are also predicted. These two spinels have a fundamental MH type band gap, and the minimum CT type band gaps (located at the Γ-point) have values of 3.43 eV and 3.82 eV, respectively. In both cases, the valence band is very flat throughout all the k-space, while the minimum of the conduction band is very pronounced for the CT band gap. Considering the effective masses calculated for the bands involving charge transfer, the electrical conductivity in these two spinels will be dominated by the conduction band electrons, especially in the case of $FeAl_2O_4$ (Table 3).

The Al spinels of Ni and Cu have indirect band gaps Γ→P and Γ→Z, respectively. Both materials have a fundamental mixed MH/CT type band gap, depending on the states involved in the valence band. In any case, the minimum charge transfer band gap values are 3.50 eV and 4.32 eV respectively, and they are located at the Γ point. Ignoring in the effective mass calculations the band formed by the empty states of Ni and Cu, we observe that both spinels have an effective electron mass of only $0.39m_e$, which points to an n-type behavior for undoped nanoporous electrodes.

In general, the CT band gaps for the entire series are rather wide, which is probably determined by the strong ionic character of the Al–O bonds, together with the fact that transition metal 3d electronic states (either full or empty) have a strongly localized character because, in spinels, the interaction between R and O orbitals is favored in an octahedral environment [89]. The spinels with a fundamental MH band gap have large electron effective masses, which results from the localized character of the states immediately above the Fermi level. Conversely, the effective masses of conduction band electrons (associated with CT band gaps) have low values throughout series. A clear trend cannot be distinguished for hole effective masses.

3.4. Band edges

Fig. 6 shows a schematic plot of the positions of the conduction and valence band edges, as well as of the center of the localized states in a potential energy scale. The position of the band edges is of outmost importance as it allows to predict the spontaneity of the hydrogen and oxygen redox processes. In this respect, it is worth noting that, in Electrochemistry, it is customary to assess spontaneity based on equilibrium

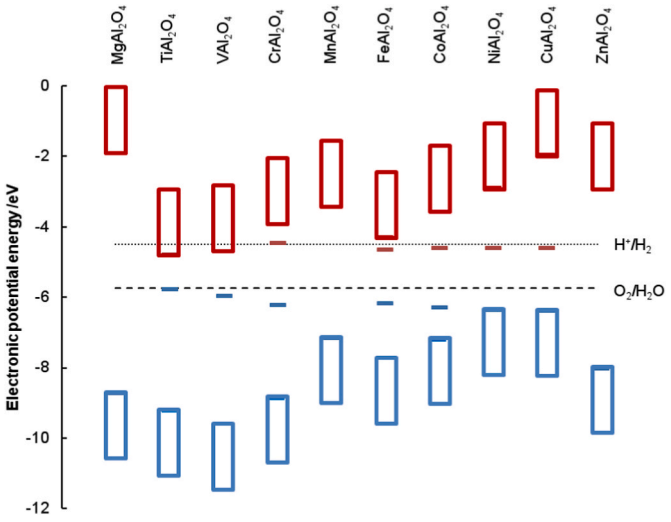

Fig. 6. Calculated band edges (with the HSE06 band gaps) for the RAl_2O_4 spinels against the redox pairs H^+/H_2 and O_2/H_2O at pH = 0.

electrode potentials rather than on the direct use of reaction Gibbs energies. In addition, in Condensed Matter Physics, instead of handling electrode potentials, it is customary to use electronic potential energies. The spontaneity criterion for electron transfer leading to hydrogen evolution is that the conduction band edge should have an energy higher than that corresponding to the energy level of the H^+/H_2 redox couple. Conversely, the spontaneity criterion for hole transfer leading to oxygen evolution is that the valence band edge should have an energy lower than that corresponding to the energy level of the O_2/H_2O redox couple.

Based on the criteria given above, all the spinels, except for $TiAl_2O_4$ and VAl_2O_4, which can only oxidize water, may drive both the oxidation and the reduction processes in water photoelectrolysis. However, for all the spinels containing transition metals, except for the Mn spinel, the band structure is not ideal because there exist highly localized electronic states (either filled or empty) in the middle of the CT band gap. Although the presence of these states gives rise to lower band gaps, this is not beneficial for water splitting. In this respect, it is critical that the photogenerated electron-hole pairs separate as quickly and efficiently as possible, first to avoid their recombination and mutual annihilation, and second to enable the minority carrier to reach the electrode interface. In this respect, electron excitations associated with a Mott-Hubbard type band gap usually correspond to promotions between d-states of the same atom, which is of little utility for water photoelectrolysis. In the same way, the presence of states in the middle of the CT band gap may lead to increased recombination. On the other hand, the CT band gap seems to be too wide in the entire series for practical purposes, above 3.0 eV in all

spinels, being only the UV portion of the solar spectrum useable. In general, in all the Al spinel series, the Al–O bonds have mainly an ionic character regardless of the transition metal involved, in agreement with very little hybridization between the d states of the transition metals and the states of other atoms, which, in turn, renders the transition metal states highly localized.

3.5. XRD structural characterization

The sol-gel procedure described in the experimental section led to the synthesis of $MgAl_2O_4$, $CoAl_2O_4$, $NiAl_2O_4$, and $ZnAl_2O_4$ spinel oxides in pure crystalline phases. All the peaks appearing in the patterns in Fig. 7 correspond to the diffractograms typical of these oxides, and no additional peaks were observed that could be attributed to other crystal phases. In contrast, no experimental evidence was found for the formation of the Ti, V, and Cr aluminum spinels. This result is not unexpected, as for these elements the oxidation state +2 is not the most stable one. In addition, the experimental conditions of the synthesis, using aqueous reaction media, and thermal treatments in air tend to favor the formation of higher oxidation states.

3.6. UV–vis characterization

For the spinels obtained as pure phases, UV–vis diffuse reflectance measurements were carried out. From the experimental spectra, by using the Kulbelka-Munk transformation, Tauc plots were obtained, allowing us to determine both the direct and the indirect band gaps (Fig. 8) given in Table 4. It is worth noting that a partial inversion of the spinel (which may occur depending on the synthesis conditions), together with a lack of stoichiometry can significantly modify the band gap values due to the presence of localized states within the band gap in the latter case [30].

For $NiAl_2O_4$ and $CoAl_2O_4$, in the Kubelka-Munk plots we can clearly distinguish absorption features in separate wavelength ranges: a band from 700 nm to 500 nm, and a main contribution below 450 nm. The first band confers a characteristic blue color to these materials, and it is due to spin-allowed transitions between the e subshell and the t_2 subshell of the transition metal. This band indicates the presence of Co^{2+} and Ni^{2+} in tetrahedral environments and does not give rise to charge separation, thus not being useful for water photoelectrolysis. On the other hand, the absorption below 450 nm is due to charge-transfer excitations from O 2p to Al 3s, Al 4p and R 4s [37,38,44,90], giving rise to charge separation. Due to the presence of defects (and probably non-stoichiometry, too), a series of localized states, both full and empty, may appear in the band gap, which gives rise to indirect transitions of lower energy than the actual indirect band gap for defect-free materials [30]. As the direct band gap values are more reliable, they are the only considered for comparison with the theoretical results. For the Ni spinel, there is very good agreement between the measured and calculated band gaps, while for the Co spinel there is good agreement for the MH band gap, but not for the CT band gap (3.82 eV calculated vs. 2.9 eV measured) (Table 4). It is also important to note that the Kubelka-Munk plots for Mg, Co, Ni, and Zn Al-spinels show a good qualitative correlation with the corresponding DOS of the conduction band.

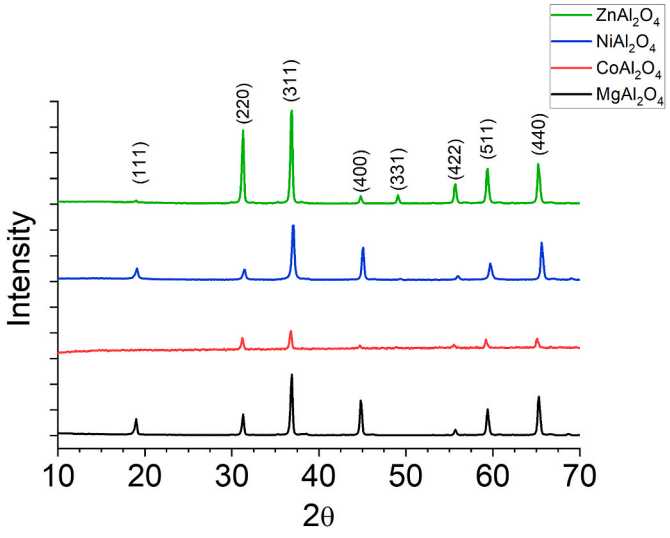

Fig. 7. XRD patterns for the spinels synthesized as pure phases using a sol-gel procedure.

3.7. Photoelectrochemical measurements

Fig. 9 shows linear voltammograms obtained under chopped white illumination for different spinel electrodes in contact with aqueous alkaline media. In all cases, modest oxidation photocurrents are obtained, indicating that these materials behave as photoanodes. Accordingly, Mott-Schottky plots obtained in the dark (see Fig. S8) show a positive slope in all cases, confirming that the spinels behave as n-type semiconductor electrodes.

The spikes observed for the Co spinel photoelectrode (and, to a lesser extent, for the Ni spinel also) are likely a consequence of hole trapping at the oxide surface, which induces an increase in recombination upon continued illumination. The transients are also characterized by negative spikes when illumination is interrupted. They are related to the recombination of conduction band electrons with the holes trapped during previous illumination. Surface hole trapping may be related to the existence of a valence band dominated by Co^{2+} states, with corresponding surface states that may act as trapping and recombination centers. Out of the four spinels synthesized, the Co spinel is the only one that has a valence band with this feature and the only one showing photocurrents with pronounced spikes.

In all four cases, the experimental photocurrent onset appears at potentials much more positive than the theoretical ones (corresponding approximately to the potential of the CB edge). This means that trapping and recombination both in the bulk and at the surface clearly hinder the performance of the photoelectrodes. Moreover, the high carrier densities calculated from the slopes of the Mott-Schottky plots (see Table S3) indicate significant deviations from the ideal stoichiometry and thus, a high defect density, which does not favor strong photoresponses. In any case, the electrodes with a lower onset potential are those containing Ni and Co. The flat-band potentials obtained from the Mott-Schottky plots (see Table S3) are in all cases significantly negative to the photocurrent onset), which confirms the existence of a high level of surface hole trapping and recombination.

3.8. Comparison of theoretical and experimental results

The R metal in RAl_2O_4 is occupying the tetrahedral sites in the normal spinel structure considered for the calculations. The Ti^{2+}, V^{2+}, and Cr^{2+} cations are too large for the tetrahedral sites, this explaining the high energy values obtained for their formation from the respective binary oxides. No indication of the presence of these spinels was obtained by XRD after attempting their synthesis. An additional factor to be considered is that the sol-gel synthesis involves a thermal treatment in air, which favors the formation of higher oxidation states for these metals. For the other metals studied, the XRD experiments showed the formation of the normal spinel phases, pure in the cases of the Mg, Zn, Ni, and Co aluminum spinels, and containing some impurities of the binary oxides in the cases of the Fe, Mn, and Cu spinels.

The analysis of the calculated DOS indicates that a common pattern for the electronic structure is found for the transition metals in this Al spinel series (the spinels of Mg and Zn, being diamagnetic band insulators). This common pattern corresponds to a band gap separating 3d states of the transition metal atom (empty for the conduction band and

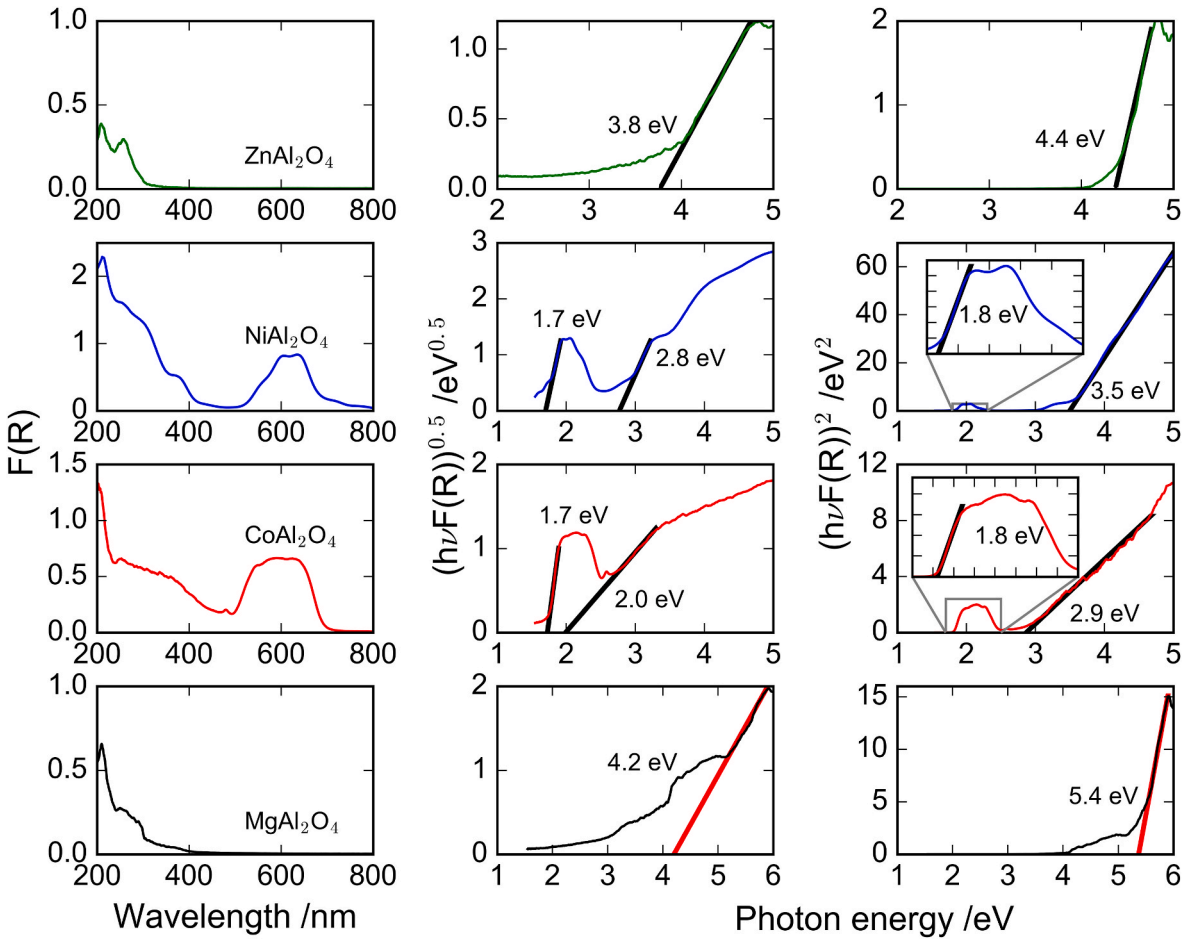

Fig. 8. Kubelka-Munk and Tauc plots for the spinels $MgAl_2O_4$, $CoAl_2O_4$, $NiAl_2O_4$ and $ZnAl_2O_4$.

Table 4
Band gap values extracted from the Tauc plots in Fig. 8 and calculated band gaps.

Spinel	Experimental band gap/eV				Calculated band gap/eV			
	Fundamental		Minimum CT		Fundamental		Minimum CT	
	Indirect	Direct	Indirect	Direct	Indirect	Direct	Indirect	Direct
$MgAl_2O_4$	4.2	5.4	–	–	–	5.2(PBE) 6.8(HSE06)	–	–
$CoAl_2O_4$	1.7	1.8	2.0	2.9	1.8	~1.8	–	3.8
$NiAl_2O_4$	1.7	1.8	2.8	3.5	1.8	~1.8	–	3.5
$ZnAl_2O_4$	3.8	4.4	–	–		3.9(PBE) 5.1(HSE06)	–	–

filled for the valence band). The transition metal Al spinels thus show an MH band gap type, except for Mn, Ni and Cu, for which a mixed MH and CT character was found. The effective masses obtained from the band edges point to the fact that these materials tend to show an n-type behavior, with significantly higher effective masses for the holes in the valence band. In addition, for some of the materials, the electronic structure indicates a highly isotropic electrical conductivity.

From the positions of the band edges, which are critical to assess whether a given material can effectively sustain photoinduced redox processes, all the spinels studied may drive under illumination both the oxidation and reduction of water, except for those of Ti and V, which would not be adequate for the reduction of water.

In the cases of the spinels of Ni and Co, the UV–vis spectra indicate the existence of excitations involving localized states at energies lower than those of the CT band gap. Accordingly, the electronic structures of both $NiAl_2O_4$ and $CoAl_2O_4$ reveal the existence of a narrow distribution of states just above the Fermi level, which participate in the definition of a MH band gap. In addition, a CT band gap is also evident for these two materials, with conduction band electrons having a much lower effective mass than that of the holes, underlying the n-type behavior observed for all the synthesized spinels in the photoelectrochemical experiments (anodic photocurrents observed at positive enough electrode potentials).

It should be noted that all of the Al spinels have relatively wide CT band gaps, above 3.0 eV, which limits their application in artificial photosynthesis. In addition, in several cases their electronic structure does not seem adequate due to the presence of strongly localized states in the middle of the charge-transfer band gap. These states give rise to coloration, which is not linked, however, to charge separation as required for photoelectrochemical applications. More work is underway to extend this type of study to other oxide families.

4. Conclusions

A DFT+U method has been developed to address the theoretical screening of aluminum-based spinels, which can be potentially extended

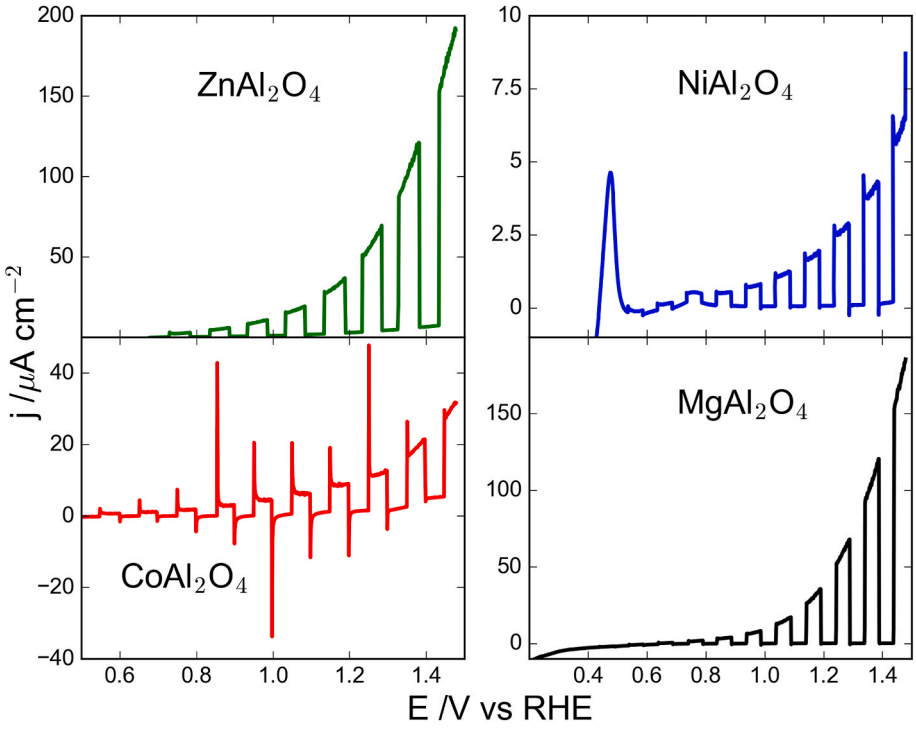

Fig. 9. Linear sweep voltammograms at 20 mV s^{-1} for different spinel electrodes under chopped illumination from the Xe(Hg) arc lamp in an N_2 purged 0.1 M NaOH electrolyte.

to other oxide families. The method uses PBE+U and HSE06 calculations to obtain tuned values for the mixing and Hubbard parameters for the divalent metal R (R: Mg, Ti–Zn) in normal spinel RAl_2O_4 oxides that (i) reproduce the experimental band gap when available (within 0.1–0.2 eV), and (ii) yield similar electronic structures (DOS) at both theory levels. It is worth noting that the values for the parameters are optimized for transition metals in the oxidation state +2 and in a tetrahedral environment. As far as we know, such U values are lacking in the literature.

The computational screening, involving calculations at the PBE, PBE+U, and HSE06 levels, yields estimates for the formation energies (from the binary oxides), electronic structure (DOS and PDOS plots), band structure, band gap types and values, and effective masses of charge carriers. A very similar electronic structure (DOS) was obtained for all the spinels in the series except for those of Mg and Zn, the gap being defined by filled and empty bands with main contributions from metal 3d levels. Charge-transfer band gaps were also obtained for higher energy values. Calculated effective masses for the charge carriers (from the PBE+U band structures) indicate that electrical conductivity should be mainly due to electrons in the conduction band, which points to an n-type behavior.

The successful synthesis of the Al-spinels with Mg, Co, Ni and Zn agrees with the calculated energies of formation from the respective binary oxides. UV–vis spectra and photoelectrochemical results for these spinels are also consistent with the theoretical electronic structure. In any case, it should be noted that, for these oxides, the electronic structure predicts charge-transfer band gaps above 3.0 eV, even for strongly colored oxides, which seriously limits their potential application as electrode materials in artificial photosynthesis. Further studies are needed to identify potential dopants (either anionic or cationic) that can lead to a significant reduction of the band gap. In any case, their application in other fields such as dark electrocatalysis is not precluded as the localized states are situated at potentials adequate for promoting either water splitting or other aqueous electrochemical reactions.

From a methodological point of view, a procedure for the DFT study of new families of oxides is presented and developed for the RAl_2O_4 family. In a more general vein, this work shows the great potential of carrying out theoretical screening calculations for guiding the development of new functional materials and, more specifically, photoelectrode materials.

Credit author statement

F.J.P.: Data curation, Formal analysis, Investigation, Methodology, Software, Validation, Visualization, Writing – original draft; **M.C.:** Data curation, Investigation, Methodology, Validation, Visualization; **T.L-V.:** Supervision, Writing – review & editing; **J.M.O.:** Conceptualization, Data curation, Formal analysis, Methodology, Resources, Software, Supervision, Writing – review & editing; **R.G:** Conceptualization, Data curation, Funding acquisition, Methodology, Project administration, Resources, Supervision, Validation, Writing – review & editing.

Data availability

The raw/processed data required to reproduce these findings are available from the corresponding authors upon request.

Declaration of competing interest

The authors declare that they have no known competing financial interests or personal relationships that could have appeared to influence the work reported in this paper.

Acknowledgments

The authors gratefully acknowledge funding from the European Union's Horizon 2020 research and innovation program under grant agreement no. 760930 (FotoH2 project). This research was also partially funded by the Ministerio de Ciencia e Innovación/Agencia Estatal de Investigación/Fondos FEDER through project PID2021-128876OB-I00 and by the Generalitat Valenciana through project PROMETEO/2020/089. F.J.P. also acknowledges the Spanish Ministry of Education for the

award of an FPU grant.

Appendix A. Supplementary data

Supplementary data to this article can be found online at https://doi.org/10.1016/j.ceramint.2023.05.003.

References

[1] M.G. Walter, E.L. Warren, J.R. McKone, S.W. Boettcher, Q. Mi, E.A. Santori, N. S. Lewis, Solar water splitting cells, Chem. Rev. 111 (2011) 5815, https://doi.org/10.1021/cr200102n.

[2] A. Cots, R. Gómez, Ytterbium modification of pristine and molybdenum-modified hematite electrodes as a strategy for efficient water splitting photoanodes, Appl. Catal. B Environ. 219 (2017) 492–500, https://doi.org/10.1016/j.apcatb.2017.07.067.

[3] A. Cots, D. Cibrev, P. Bonete, R. Gómez, Photoelectrochemical behavior of molybdenum-modified nanoparticulate hematite electrodes, J. Solid State Electrochem. 22 (2018) 149–156, https://doi.org/10.1007/s10008-017-3729-6.

[4] A. Cots, D. Cibrev, P. Bonete, R. Gómez, Hematite nanorod electrodes modified with molybdenum: photoelectrochemical studies, Chemelectrochem 4 (2017) 585–593, https://doi.org/10.1002/celc.201600644.

[5] S. Kment, F. Riboni, S. Pausova, L. Wang, L. Wang, H. Han, Z. Hubicka, J. Krysa, P. Schmuki, R. Zboril, Photoanodes based on TiO_2 and α-Fe_2O_3 for solar water splitting-superior role of 1D nanoarchitectures and of combined heterostructures, Chem. Soc. Rev. 46 (2017) 3716–3769, https://doi.org/10.1039/c6cs00015k.

[6] P. Sharma, J.W. Jang, J.S. Lee, Key strategies to advance the photoelectrochemical water splitting performance of α-Fe_2O_3 photoanode, ChemCatChem 11 (2019) 157–179, https://doi.org/10.1002/cctc.201801187.

[7] J.H. Kim, Y.J. Jang, J.H. Kim, J.W. Jang, S.H. Choi, J.S. Lee, Defective $ZnFe_2O_4$ nanorods with oxygen vacancy for photoelectrochemical water splitting, Nanoscale 7 (2015) 19144–19151, https://doi.org/10.1039/c5nr05812k.

[8] M. Shahid, L. Jingling, Z. Ali, I. Shakir, M.F. Warsi, R. Parveen, M. Nadeem, Photocatalytic degradation of methylene blue on magnetically separable $MgFe_2O_4$ under visible light irradiation, Mater. Chem. Phys. 139 (2013) 566–571, https://doi.org/10.1016/j.matchemphys.2013.01.058.

[9] Y. Hou, F. Zuo, A. Dagg, P. Feng, A three-dimensional branched cobalt-doped α-Fe_2O_3 nanorod/$MgFe_2O_4$ heterojunction array as a flexible photoanode for efficient photoelectrochemical water oxidation, Angew. Chem. Int. Ed. 52 (2013) 1248–1252, https://doi.org/10.1002/anie.201207578.

[10] S. Hussain, S. Hussain, A. Waleed, M.M. Tavakoli, Z. Wang, S. Yang, Z. Fan, M. A. Nadeem, Fabrication of $CuFe_2O_4$/α-Fe_2O_3 composite thin films on FTO coated glass and 3-D nanospike structures for efficient photoelectrochemical water splitting, ACS Appl. Mater. Interfaces 8 (2016) 35315–35322, https://doi.org/10.1021/acsami.6b12460.

[11] S.J.A. Moniz, C.S. Blackman, P. Southern, P.M. Weaver, J. Tang, C.J. Carmalt, Visible-light driven water splitting over $BiFeO_3$ photoanodes grown via the LPCVD reaction of $[Bi(OtBu)_3]$ and $[Fe(OtBu)_3]_2$ and enhanced with a surface nickel oxygen evolution catalyst, Nanoscale 7 (2015) 16343–16353, https://doi.org/10.1039/c5nr04804d.

[12] Y. Gao, T.W. Hamann, Quantitative hole collection for photoelectrochemical water oxidation with $CuWO_4$, Chem. Commun. 53 (2017) 1285–1288, https://doi.org/10.1039/c6cc09029j.

[13] M. Kölbach, I.J. Pereira, K. Harbauer, P. Plate, K. Höflich, S.P. Berglund, D. Friedrich, R. Van De Krol, F.F. Abdi, Revealing the performance-limiting factors in α-$SnWO_4$ photoanodes for solar water splitting, Chem. Mater. 30 (2018) 8322–8331, https://doi.org/10.1021/acs.chemmater.8b03883.

[14] D.K. Lee, D. Lee, M.A. Lumley, K.S. Choi, Progress on ternary oxide-based photoanodes for use in photoelectrochemical cells for solar water splitting, Chem. Soc. Rev. 48 (2019) 2126–2157, https://doi.org/10.1039/c8cs00761f.

[15] F.F. Abdi, A. Chemseddine, S.P. Berglund, R. Van De Krol, Assessing the suitability of iron Tungstate (Fe_2WO_6) as a photoelectrode material for water oxidation, J. Phys. Chem. C 121 (2017) 153–160, https://doi.org/10.1021/acs.jpcc.6b10695.

[16] J.H. Kim, J.S. Lee, Elaborately modified $BiVO_4$ photoanodes for solar water splitting, Adv. Mater. 31 (2019) 1–35, https://doi.org/10.1002/adma.201806938.

[17] J. Quiñonero, T. Lana-Villarreal, R. Gómez, Improving the photoactivity of bismuth vanadate thin film photoanodes through doping and surface modification strategies, Appl. Catal. B Environ. 194 (2016) 141–149, https://doi.org/10.1016/j.apcatb.2016.04.057.

[18] J. Quiñonero, R. Gómez, Controlling the amount of co-catalyst as a critical factor in determining the efficiency of photoelectrodes: the case of nickel (II) hydroxide on vanadate photoanodes, Appl. Catal. B Environ. 217 (2017) 437–447, https://doi.org/10.1016/j.apcatb.2017.06.005.

[19] K. Song, H. Hou, C. Gong, F. Gao, D. Zhang, F. Zhi, W. Yang, F. He, Enhanced solar water splitting of $BiVO_4$ photoanodes by in situ surface band edge modulation, J. Mater. Chem. (2022) 22561–22570, https://doi.org/10.1039/d2ta06141d.

[20] K. Song, F. He, E. Zhou, L. Wang, H. Hou, W. Yang, Boosting solar water oxidation activity of $BiVO_4$ photoanode through an efficient in-situ selective surface cation exchange strategy, J. Energy Chem. 68 (2022) 49–59, https://doi.org/10.1016/j.jechem.2021.11.024.

[21] W. Yang, J. Moon, Recent advances in earth-abundant photocathodes for photoelectrochemical water splitting, ChemSusChem 12 (2019), https://doi.org/10.1002/cssc.201801554, 1889–1899.

[22] M.I. Díez-García, V. Celorrio, L. Calvillo, D. Tiwari, R. Gómez, D.J. Fermín, YFeO3 photocathodes for hydrogen evolution, electrochim, Acta 246 (2017) 365–371, https://doi.org/10.1016/j.electacta.2017.06.025.

[23] M.I. Díez-García, R. Gómez, Metal doping to enhance the photoelectrochemical behavior of $LaFeO_3$ photocathodes, ChemSusChem 10 (2017) 2457–2463, https://doi.org/10.1002/cssc.201700166.

[24] M.I. Díez-García, R. Gómez, Investigating water splitting with CaFe2O4 photocathodes by electrochemical impedance spectroscopy, ACS Appl. Mater. Interfaces 8 (2016) 21387–21397, https://doi.org/10.1021/acsami.6b07465.

[25] M.I. Díez-García, T. Lana-Villarreal, R. Gómez, Study of copper ferrite as a novel photocathode for water reduction: improving its photoactivity by electrochemical pretreatment, ChemSusChem 9 (2016) 1504–1512, https://doi.org/10.1002/cssc.201600023.

[26] M.S. Prévot, X.A. Jeanbourquin, W.S. Bourée, F. Abdi, D. Friedrich, R. Van De Krol, N. Guijarro, F. Le Formal, K. Sivula, Evaluating charge carrier transport and surface states in $CuFeO_2$ photocathodes, Chem. Mater. 29 (2017) 4952–4962, https://doi.org/10.1021/acs.chemmater.7b01284.

[27] A.K. Díaz-García, T. Lana-Villarreal, R. Gómez, Sol-gel copper chromium delafossite thin films as stable oxide photocathodes for water splitting, J. Mater. Chem. A. 3 (2015) 19683–19687, https://doi.org/10.1039/c5ta05227k.

[28] A. Hever, C. Oses, S. Curtarolo, O. Levy, A. Natan, The structure and composition statistics of 6A binary and ternary crystalline materials, Inorg. Chem. 57 (2018) 653–667, https://doi.org/10.1021/acs.inorgchem.7b02462.

[29] M. Woodhouse, B.A. Parkinson, Combinatorial discovery and optimization of a complex oxide with water photoelectrolysis activity, Chem. Mater. 20 (2008) 2495–2502, https://doi.org/10.1021/cm703099j.

[30] N. Pathak, P.S. Ghosh, S.K. Gupta, S. Mukherjee, R.M. Kadam, A. Arya, An insight into the various defects-induced emission in $MgAl_2O_4$ and their tunability with phase behavior: combined experimental and theoretical approach, J. Phys. Chem. C 120 (2016) 4016–4031, https://doi.org/10.1021/acs.jpcc.5b11822.

[31] Q. Li, T. Liu, X. Xu, X. Wang, R. Guo, X. Jiao, Y. Lu, Study on the optical spectra of $MgAl_2O_4$ with oxygen vacancies, Mater. Technol. 36 (2021) 279–285, https://doi.org/10.1080/10667857.2020.1750163.

[32] O. Shtyka, W. Maniukiewicz, R. Ciesielski, A. Kedziora, V. Shatsila, T. Sierański, T. Maniecki, The formation of Cr-Al spinel under a reductive atmosphere, Materials 14 (2021), https://doi.org/10.3390/ma14123218.

[33] S. Wang, X. Wei, H. Gao, Y. Wei, Effect of amorphous alumina and α-alumina on optical, color, fluorescence properties and photocatalytic activity of the $MnAl_2O_4$ spinel oxides, Optik 185 (2019) 301–310, https://doi.org/10.1016/j.ijleo.2019.03.147.

[34] S. Suguna, S. Shankar, S.K. Jaganathan, A. Manikandan, Novel synthesis of spinel $Mn_xCo_{1-x}Al_2O_4$ (x = 0.0 to 1.0) nanocatalysts: effect of Mn^{2+} doping on structural, morphological, and opto-magnetic properties, J. Supercond. Nov. Magnetism 30 (2017) 691–699, https://doi.org/10.1007/s10948-016-3866-7.

[35] H.Y. Mu, F.T. Li, X.T. An, R.H. Liu, Y.L. Li, X. Qian, Y.Q. Hu, One-step synthesis, electronic structure, and photocatalytic activity of earth-abundant visible-light-driven $FeAl_2O_4$, Phys. Chem. Chem. Phys. 19 (2017) 9392–9401, https://doi.org/10.1039/c7cp01007a.

[36] S. Boudiaf, N. Nasrallah, M. Mellal, C. Belabed, B. Belhamdi, D. Meziani, B. Mehdi, M. Trari, Synthesis and characterization of semiconductor $CoAl_2O_4$ for optical and dielectric studies: application to photodegradation of organic pollutants under visible light, Optik 219 (2020), 165038, https://doi.org/10.1016/j.ijleo.2020.165038.

[37] R. Jagadeeshwaran, C. Murugaraj, Structural, optical, magnetic, and electrical properties of $Ni_{0.5}Co_{0.5}Al_2O_4$ system, J. Supercond. Nov. Magnetism 33 (2020) 1765–1772.

[38] M.E. Gouda, W.A.A. Bayoumy, Structural, optical and magnetic properties of Ni-aluminates with Co substitution, Int. J. Sci. Eng. Res. 6 (2015) 328–333.

[39] S.D. Mekkey, M.E. Sultan, M.M. Elsenety, A. Helal, B.A. Elsayed, Photocatalytic degradation of rhodamine B in the visible region using nanostructured $CoAl_{2-x}La_xO_4$ (x = 0, 0.01, 0.03, 0.07, and 0.09) series: photocatalytic activity and DFT calculations, Inorg. Chem. Commun. 136 (2022), 109176, https://doi.org/10.1016/j.inoche.2021.109176.

[40] A. Irshad, M. Shahid, S.M. El-Bahy, I.H. El Azab, G.A.M. Mersal, M.M. Ibrahim, P. O. Agboola, I. Shakir, Nickel doped $CoAl_2O_4$@CNT nanocomposite: synthesis, characterization, and evaluation of sunlight driven catalytic studies, Phys. B Condens. Matter 636 (2022), 413873, https://doi.org/10.1016/j.physb.2022.413873.

[41] I. Sebai, N. Salhi, G. Rekhila, M. Trari, Visible light induced H_2 evolution on the spinel $NiAl_2O_4$ prepared by nitrate route, Int. J. Hydrogen Energy 42 (2017) 26652–26658, https://doi.org/10.1016/j.ijhydene.2017.09.092.

[42] V. Elakkiya, Y. Agarwal, S. Sumathi, Photocatalytic activity of divalent ion (copper, zinc and magnesium) doped $NiAl_2O_4$, Solid State Sci. 82 (2018) 92–98, https://doi.org/10.1016/j.solidstatesciences.2018.06.008.

[43] S. Jayasree, A. Manikandan, S.A. Antony, A.M. Uduman Mohideen, C. Barathiraja, Magneto-optical and catalytic properties of recyclable spinel $NiAl_2O_4$ nanostructures using facile combustion methods, J. Supercond. Nov. Magnetism 29 (2016) 253–263, https://doi.org/10.1007/s10948-015-3249-5.

[44] T. Tangcharoen, J. T-Thienprasert, C. Kongmark, Effect of calcination temperature on structural and optical properties of MAl_2O_4 (M = Ni, Cu, Zn) aluminate spinel nanoparticles, J. Adv. Ceram. 8 (2019) 352–366, https://doi.org/10.1007/s40145-019-0317-5.

[45] R. Chellammal Gayathri, V. Elakkiya, S. Sumathi, Effect of method of preparation on the photocatalytic activity of $NiAl_2O_4$, Inorg. Chem. Commun. 129 (2021), 108634, https://doi.org/10.1016/j.inoche.2021.108634.

[46] M. Arunkumar, A.S. Nesaraj, One pot chemical synthesis of ultrafine $NiAl_2O_4$ nanoparticles: physico-chemical properties and photocatalytic degradation of organic dyes under visible light irradiation, Inorg. Nano-Metal Chem. 51 (2021) 910–917, https://doi.org/10.1080/24701556.2020.1813173.

[47] J. Yanyan, L. Jinggang, S. Xiaotao, N. Guiling, W. Chengyu, G. Xiumei, $CuAl_2O_4$ powder synthesis by sol-gel method and its photodegradation property under visible light irradiation, J. Sol. Gel Sci. Technol. 42 (2007) 41–45, https://doi.org/10.1007/s10971-006-1525-3.

[48] F.Z. Akika, M. Benamira, H. Lahmar, M. Trari, I. Avramova, Suzer, Structural and optical properties of Cu-doped $ZnAl_2O_4$ and its application as photocatalyst for Cr (VI) reduction under sunlight, Surface. Interfac. 18 (2020), 100406, https://doi.org/10.1016/j.surfin.2019.100406.

[49] S.A. Hassanzadeh-Tabrizi, R. Pournajaf, A. Moradi-Faradonbeh, S. Sadeghinejad, Nanostructured $CuAl_2O_4$: Co-precipitation synthesis, optical and photocatalytic properties, Ceram. Int. 42 (2016) 14121–14125, https://doi.org/10.1016/j.ceramint.2016.06.026.

[50] M. Salavati-Niasari, F. Davar, M. Farhadi, Synthesis and characterization of spinel-type $CuAl_2O_4$ nanocrystalline by modified sol-gel method, J. Sol. Gel Sci. Technol. 51 (2009) 48–52, https://doi.org/10.1007/s10971-009-1940-3.

[51] J. Zhang, J. Xin, C. Shao, X. Li, X. Li, S. Liu, Y. Liu, Direct Z-scheme heterostructure of p-$CuAl_2O_4$/n-Bi_2WO_6 composite nanofibers for efficient overall water splitting and photodegradation, J. Colloid Interface Sci. 550 (2019) 170–179, https://doi.org/10.1016/j.jcis.2019.04.099.

[52] J. Zhang, C. Shao, X. Li, J. Xin, R. Tao, Y. Liu, Assembling n-Bi_2MoO_6 nanosheets on electrospun p-$CuAl_2O_4$ hollow nanofibers: enhanced photocatalytic activity based on highly efficient charge separation and transfer, ACS Sustain. Chem. Eng. 6 (2018) 10714–10723, https://doi.org/10.1021/acssuschemeng.8b02040.

[53] M.M. Kaci, N. Nasrallah, A.M. Djaballah, I. Akkari, C. Belabed, A. Soukeur, F. Atmani, M. Trari, Insights into the optical and electrochemical features of $CuAl_2O_4$ nanoparticles and it use for methyl violet oxidation under sunlight exposure, Opt. Mater. 126 (2022), 112198, https://doi.org/10.1016/j.optmat.2022.112198.

[54] I. Suhariadi, Y. Rahmawan, D.A.M. Muyassiroh, M.A. Barrinaya, J.F. Fatriansyah, Low-temperature deposition of $CuAl_2O_4$ thin film photocatalyst by ultrasonic spray pyrolysis, Mater. Lett. 311 (2022), 131620, https://doi.org/10.1016/j.matlet.2021.131620.

[55] S. Naghibi, A. Basravi, Y. Tang, Crystal growth, optical properties, and photocatalytic performances of ZnO-$CuAl_2O_4$ hybrid compounds: theoretical and experimental studies, Cryst. Res. Technol. 57 (2022) 1–11, https://doi.org/10.1002/crat.202100128.

[56] S.N. Ogugua, O.M. Ntwaeaborwa, H.C. Swart, Luminescence, structure and insight on the inversion degree from normal to inverse spinel in a $ZnAl_{(2-x)}Fe_x^{3+}O_4$ system, Bol. Soc. Esp. Ceram. Vidr. 60 (2020) 147–162, https://doi.org/10.1016/j.bsecv.2020.02.005.

[57] T. Sofia Nirmala, N. Iyandurai, S. Yuvaraj, M. Sundararajan, Effect of Cu^{2+} ions on structural, morphological, optical and magnetic behaviors of $ZnAl_2O_4$ spinel, Mater. Res. Express 7 (2020) 0–9, https://doi.org/10.1088/2053-1591/ab7a7a.

[58] I.E. Castelli, T. Olsen, S. Datta, D.D. Landis, S. Dahl, K.S. Thygesen, K.W. Jacobsen, Computational screening of perovskite metal oxides for optimal solar light capture, Energy Environ. Sci. 5 (2012) 5814–5819, https://doi.org/10.1039/c1ee02717d.

[59] I.E. Castelli, D.D. Landis, K.S. Thygesen, S. Dahl, I. Chorkendorff, T.F. Jaramillo, K. W. Jacobsen, New cubic perovskites for one- and two-photon water splitting using the computational materials repository, Energy Environ. Sci. 5 (2012) 9034–9043, https://doi.org/10.1039/c2ee22341d.

[60] I.E. Castelli, K.S. Thygesen, K.W. Jacobsen, Bandgap engineering of double perovskites for one- and two-photon water splitting, Mater. Res. Soc. Symp. Proc. 1523 (2013) 18–23, https://doi.org/10.1557/opl.2013.450.

[61] I.E. Castelli, J.M. García-Lastra, F. Hüser, K.S. Thygesen, K.W. Jacobsen, Stability and bandgaps of layered perovskites for one- and two-photon water splitting, New J. Phys. 15 (2013), https://doi.org/10.1088/1367-2630/15/10/105026.

[62] K. Kuhar, A. Crovetto, M. Pandey, K.S. Thygesen, B. Seger, P.C.K. Vesborg, O. Hansen, I. Chorkendorff, K.W. Jacobsen, Sulfide perovskites for solar energy conversion applications: computational screening and synthesis of the selected compound $LaYS_3$, Energy Environ. Sci. 10 (2017) 2579–2593, https://doi.org/10.1039/c7ee02702h.

[63] M. Pandey, K.W. Jacobsen, Promising quaternary chalcogenides as high-band-gap semiconductors for tandem photoelectrochemical water splitting devices: a computational screening approach, Phys. Rev. Mater. 2 (2018) 23–32, https://doi.org/10.1103/PhysRevMaterials.2.105402.

[64] Y. Wu, P. Lazic, G. Hautier, K. Persson, G. Ceder, First principles high throughput screening of oxynitrides for water-splitting photocatalysts, Energy Environ. Sci. 6 (2013) 157–168, https://doi.org/10.1039/c2ee23482c.

[65] S.M. Xu, T. Pan, Y.B. Dou, H. Yan, S.T. Zhang, F.Y. Ning, W.Y. Shi, M. Wei, Theoretical and experimental study on $M^{II}M^{III}$-layered double hydroxides as efficient photocatalysts toward oxygen evolution from water, J. Phys. Chem. C 119 (2015), 18823, https://doi.org/10.1021/acs.jpcc.5b01819. –18834.

[66] S. Li, M. Shi, J. Yu, S. Li, S. Lei, L. Lin, J. Wang, Two-dimensional blue-phase CX (X = S, Se) monolayers with high carrier mobility and tunable photocatalytic water splitting capability, Chin. Chem. Lett. 32 (2021) 1977–1982, https://doi.org/10.1016/J.CCLET.2020.09.056.

[67] J. Wang, X. Yang, J. Cao, Y. Wang, Q. Li, Computational study of the electronic, optical and photocatalytic properties of single-layer hexagonal zinc chalcogenides, Comput. Mater. Sci. 150 (2018) 432–438, https://doi.org/10.1016/J.COMMATSCI.2018.04.049.

[68] A. Jain, G. Hautier, C.J. Moore, S. Ping Ong, C.C. Fischer, T. Mueller, K.A. Persson, G. Ceder, A high-throughput infrastructure for density functional theory calculations, Comput. Mater. Sci. 50 (2011) 2295–2310, https://doi.org/10.1016/j.commatsci.2011.02.023.

[69] M. Aykol, C. Wolverton, Local environment dependent GGA+U method for accurate thermochemistry of transition metal compounds, Phys. Rev. B Condens. Matter 90 (2014) 1–18, https://doi.org/10.1103/PhysRevB.90.115105.

[70] G. Hautier, S.P. Ong, A. Jain, C.J. Moore, G. Ceder, Accuracy of density functional theory in predicting formation energies of ternary oxides from binary oxides and its implication on phase stability, Phys. Rev. B Condens. Matter 85 (2012) 155208, https://doi.org/10.1103/PhysRevB.85.155208.

[71] J. He, C. Franchini, Screened hybrid functional applied to $3d^0 \rightarrow 3d^8$ transition-metal perovskites $LaMO_3$ (M=Sc-Cu): influence of the exchange mixing parameter on the structural, electronic, and magnetic properties, Phys. Rev. B Condens. Matter 86 (2012), https://doi.org/10.1103/PhysRevB.86.235117.

[72] G. Kresse, J. Furthmüller, Efficient iterative schemes for ab initio total-energy calculations using a plane-wave basis set, Phys. Rev. B Condens. Matter 54 (1996) 11169–11186, https://doi.org/10.1103/PhysRevB.54.11169.

[73] P.E. Blöchl, Projector augmented-wave method, Phys. Rev. B 50 (1994) 17953–17979, https://doi.org/10.1103/PhysRevB.50.17953.

[74] G. Kresse, D. Joubert, From ultrasoft pseudopotentials to the projector augmented-wave method, Phys. Rev. B Condens. Matter 59 (1999) 1758–1775, https://doi.org/10.1103/PhysRevB.59.1758.

[75] J.P. Perdew, K. Burke, M. Ernzerhof, Generalized gradient approximation made simple, Phys. Rev. Lett. 77 (1996) 3865–3868, https://doi.org/10.1103/PhysRevLett.77.3865.

[76] S.L. Dudarev, G.A. Botton, S.Y. Savrasov, C.J. Humphreys, A.P. Sutton, Electron-energy-loss Spectra and the Structural Stability of Nickel Oxide: an LSDA+U Study, vol. 57, 1997, p. 5.

[77] J. Heyd, G.E. Scuseria, M. Ernzerhof, Hybrid functionals based on a screened Coulomb potential, J. Chem. Phys. 118 (2003) 8207–8215, https://doi.org/10.1063/1.1564060.

[78] T. Arima, Y. Tokura, J.B. Torrance, Variation of optical gaps in perovskite-type 3d transition-metal oxides, Phys. Rev. B 48 (1993) 17006–17009, https://doi.org/10.1103/PhysRevB.48.17006.

[79] Z. Song, Q. Liu, Tolerance factor and phase stability of the normal spinel structure, Cryst. Growth Des. 20 (2020) 2014–2018, https://doi.org/10.1021/acs.cgd.9b01673.

[80] I. Elias, A. Soon, J. Huang, B.S. Haynes, A. Montoya, Atomic order, electronic structure and thermodynamic stability of nickel aluminate, Phys. Chem. Chem. Phys. 21 (2019) 25952–25961, https://doi.org/10.1039/c9cp04325j.

[81] C. Otero Arean, J.S. Diez Viniuela, Structural study of copper-nickel (CuxNi1-xAl2O4) spinels aluminate, J. Solid State Chem. 60 (1985) 1–5.

[82] V. Singh, M. Kosa, K. Majhi, D.T. Major, Putting DFT to the test: a first-principles study of electronic, magnetic, and optical properties of Co_3O_4, J. Chem. Theor. Comput. 11 (2015) 64–72, https://doi.org/10.1021/ct500770m.

[83] K. Izumi, T. Mizokawa, E. Hanamura, Optical response and electronic structure of Zn-doped $MgAl_2O_4$, J. Appl. Phys. 102 (2007), 053109, https://doi.org/10.1063/1.2777528.

[84] X.C. Huang, J.Y. Zhang, M. Wu, S. Zhang, H.Y. Xiao, W.Q. Han, T.L. Lee, A. Tadich, D.C. Qi, L. Qiao, L. Chen, K.H.L. Zhang, Electronic structure and p -type conduction mechanism of spinel cobaltite oxide thin films, Phys. Rev. B 100 (2019) 1–9, https://doi.org/10.1103/PhysRevB.100.115301.

[85] G. Ertl, R. Hierl, H. Knözinger, N. Thiele, H.P. Urbach, XPS study of copper aluminate catalysts, Appl. Surf. Sci. 5 (1980) 49–64, https://doi.org/10.1016/0378-5963(80)90117-8.

[86] Q. Zhong, F.S. Ohuchi, Surface science studies on the Ni/Al_2O_3 interface, J. Vac. Sci. Technol. A Vacuum, Surfaces, Film. 8 (1990) 2107–2112, https://doi.org/10.1116/1.577011.

[87] S. Akbudak, A.K. Kushwaha, G. Uğur, Uğur, H.Y. Ocak, Structural, electronic, elastic, optical and vibrational properties of MAl_2O_4 (M = Co and Mn) aluminate spinels, Ceram. Int. 44 (2018) 310–316, https://doi.org/10.1016/j.ceramint.2017.09.174.

[88] A. Walsh, S.H. Wei, Y. Yan, M.M. Al-Jassim, J.A. Turner, M. Woodhouse, B. A. Parkinson, Structural, magnetic, and electronic properties of the Co-Fe-Al oxide spinel system: density-functional theory calculations, Phys. Rev. B Condens. Matter 76 (2007) 1–9, https://doi.org/10.1103/PhysRevB.76.165119.

[89] S. Sun, Y. Sun, Y. Zhou, S. Xi, X. Ren, B. Huang, H. Liao, L.P. Wang, Y. Du, Z.J. Xu, Shifting oxygen charge towards octahedral metal: a way to promote water oxidation on cobalt spinel oxides, Angew. Chem. 131 (2019) 6103–6108, https://doi.org/10.1002/ange.201902114.

[90] C. Maurizio, N. El Habra, G. Rossetto, M. Merlini, E. Cattaruzza, L. Pandolfo, M. Casarin, XAS and GIXRD study of Co sites in $CoAl_2O_4$ layers grown by MOCVD, Chem. Mater. 22 (2010) 1933–1942, https://doi.org/10.1021/cm9018106.